Preprints of the 20th World Congress
The International Federation of Automatic Control
Toulouse, France, July 9-14, 2017

Design and 3D Motion Modeling of a 300-m Gliding Robotic Dolphin ⋆

Jun Yuan, [*,**] **Zhengxing Wu,** [**] **Junzhi Yu,** [**] **Chao Zhou,** [**] **and Min Tan** [**]

[*] *University of Chinese Academy of Sciences, Beijing, 100049, China (e-mail: yuanjun2012@ia.ac.cn)*
[**] *State Key Laboratory of Management and Control for Complex Systems, Institute of Automation, Chinese Academy of Sciences, Beijing, 100190, China (e-mail: zhengxing.wu@ia.ac.cn, junzhi.yu@ia.ac.cn, chao.zhou@ia.ac.cn, min.tan@ia.ac.cn)*

Abstract: This paper presents the mechatronic design and three-dimensional (3D) motion modeling of a gliding robotic dolphin capable of diving as deep as 300 m. Propulsion modes of bio-inspired robotic dolphin and traditional underwater gliders are integrated into the robot in order to endow it with both high maneuverability and long endurance simultaneously. It is realized by introducing a buoyancy adjusting mechanism on the basis of a bio-inspired robotic dolphin. Particular design on mechanical seal and compressive strength is implemented to achieve large diving depth. Further, a full-state dynamic model for 3D gliding motion is established for motion analysis. In comparison with traditional underwater gliders, the robot's flippers and fluke are controllable and thereby enrich the state-regulating modes of gliding motion, which is considered specially in the dynamic model. Simulations are conducted to analyze the robot's 3D gliding motion. Experiments are also carried out to validate the robot's gliding performance and the effectiveness of the formulated dynamic model.

Keywords: Underwater robotics, dynamic modeling, motion control, gliding robotic dolphin, mechatronic design.

1. INTRODUCTION

Biological evolution and natural selection endow dolphins with extraordinary swimming skills (Weihs (2002)). How to endow underwater robots with dolphin-like locomotion performance is a topic that has aroused great research interests in recent years. Researches on bio-inspired robotic dolphin (Nakashima et al. (2006); Yu et al. (2012, 2016)) are promising approaches. For instance, Yu et al. (2016) implemented a robotic dolphin with a fast swimming speed (2.07 m/s or 2.9 BL/s, BL for body length) and replicated acrobatic-like dolphin leaping behaviors based on an integrative control method. With the improvement of mechatronic systems and control algorithms, speed and maneuverability of robotic dolphins also evolves. In spite of their excellent swimming performance and distinctive characteristics, limited endurance is a flaw that prevents them from practical applications.

In terms of endurance and range, underwater gliders (Eriksen et al. (2001); Schofield et al. (2007); Leonard et al. (2010)) have overwhelming advantage over other underwater robots or vehicles. In general, gliders are able to glide for thousands of kilometers and sustain motion for several months or even years without charging. Such astonishing energy-efficiency is attributed to the buoyancy-driven mechanism. Their thrust is generated by the combined action of net buoyancy and hydrodynamic forces, rather than screw propellers commonly used in traditional underwater vehicles. Ideally, energy is only consumed when they adjust their buoyancy to switch between surfacing and diving. However, gliders' propulsion mode determines that their speed and maneuverability are much lower and they are not suitable for applications which demand high speed and maneuverability.

Therefore, the concept of gliding robotic dolphin (Wu et al. (2015a)) was proposed in order to achieve high maneuverability and long endurance simultaneously, via combining the propulsive mechanisms of both robotic dolphin and underwater gliders. The gliding robotic dolphin can switch between swimming and gliding as required. Specially, the two kind of propulsive mechanisms are not isolated from each other, but can enrich each other's control mode. The design diving depth of the gliding robotic dolphin in (Wu et al. (2015a)) was 20 m and only 2D gliding motion in the vertical plane was analyzed.

This paper focuses on the mechatronic design and 3D motion modeling of an improved gliding robotic dolphin capable of diving as deep as 300 m. Particular design on mechanical seal and compressive strength is conducted to achieve large dive depth. Further, a full-state dynamic model for 3D gliding motion are established for motion analysis. In comparison with traditional underwater glid-

⋆ This work was supported by the National Natural Science Foundation of China (nos. 61603388, 61375102, 61633017 and 61421004), the Beijing Natural Science Foundation (nos. 3141002 and 4164103), and by the Early Career Development Award of SKLMCCS.

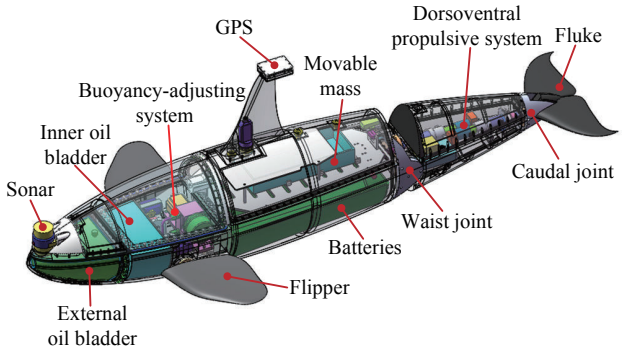

Fig. 1. Mechanical structure of the developed gliding robotic dolphin.

ers, the robot's flippers and fluke are controllable and versatile actuators for regulating motion states, which is considered particularly during dynamic modeling. Simulations are implemented to analyze the robot's 3D gliding motion. Experiments are also carried out to verify the robot's gliding performance and the effectiveness of the derived dynamic model.

The remainder of the paper is organized as follows. Section 2 presents the mechatronic design of the robot. Thereafter, we derives the dynamic model for 3D gliding motion in Section 3. In Section 4, the results of simulations and experiments are elaborated. Finally, Section 5 concludes this paper.

2. MECHATRONIC DESIGN

The mechanical structure of the gliding robotic dolphin is shown in Fig. 1. The total length and mass are 1.5 m and 58.1 kg, respectively. Inspired by the biological drag reduction mechanism of underwater creatures, we employ the streamlined profile of a killer whale to design the entire geometric shape of the robot. Just as fins are indispensable organs for dolphins to implement any locomotion, the flippers and the fluke own equivalent significance for the robot. The robot's hull is made of aluminum alloy to ensure sufficient compressive strength. Four integrated mechanical systems enable the robot to realize swimming and gliding, including a dorsoventral propulsive system, a buoyancy adjusting system, a pitch adjusting system, and a pair of controllable flippers.

Similar to a dolphin's agile tail, the dorsoventral propulsive system generates rhythmical dorsoventral oscillations to achieve dolphin-like swimming. The fluke, the waist joint, the caudal joint and two groups of drive mechanisms constitute the system. The two joints are powered by motors to drive the caudal cabinet and the fluke to stroke surrounding water vertically. The fluke provides most of the thrust during swimming, while it can also be used for adjusting attitude during gliding.

The buoyancy adjusting system endows the robot with the capability of gliding. The system consists of a pump, a solenoid valve, two oil bladders, and pipelines. The two bladders are placed inside and outside the hull, respectively. Indeed, the external one is exposed to water, although it is covered and protected by a fairing. When the pump ejects or sucks oil, the external bladder's volume and

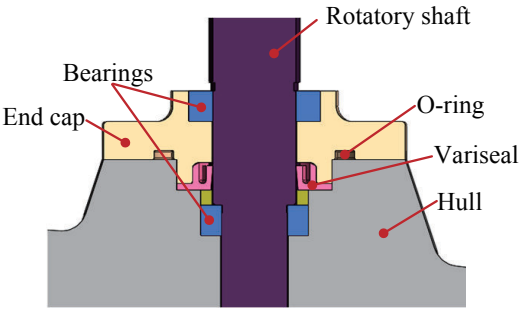

Fig. 2. Mechanical seal design for a rotatory shaft.

the robot's buoyancy concurrently changes. Thereby, the gliding direction (upwards or downwards) also changes.

The pitch adjusting system works by shifting a movable mass longitudinally. A battery group acts as the mass to conserve internal space. In addition, the pair of flippers are also versatile fin surfaces: adjusting attitude during gliding or swimming, and flapping continuously for MPF (median and/or paired fin) locomotion (Wu et al. (2015b)). Each flipper is with one-degree-of-freedom (1-DOF) and driven by a servomotor to rotate in $[-90°, 90°]$.

From the perspective of mechanical design, the gliding robotic dolphin is a product that merely introduces the buoyancy adjusting system on the basis of traditional robotic dolphin. In essence, it is due to that robotic dolphins possess innate potential of being remoulded to be underwater gliders:

(1) The streamlined geometric profiles of the body, the flippers as well as the fluke can provide necessary and adequate lift-to-drag ratio for gliding motion.
(2) The flippers and the fluke can play the role of control surfaces and regulate the attitude for gliding motion.

Certainly, the buoyancy adjusting system can endow the robot with the ability of diving or surfacing without the assistance of flippers during swimming.

Particular design on mechanical seal enables the robot to dive as deep as 300 m. O-rings are applied to static seal of the hull. The mechanical seal design of a rotatory shaft is more challenging, as illustrated in Fig. 2. The crucial seal is a variseal with its cavity facing against the water pressure. The larger is the water pressure, the tighter the cavity's walls squeeze to the end cap and the shaft, to prevent the water from passing through. The variseal is made of PTEF (polytetrafluoroethylene) for its remarkable wear resistance. In addition, the shaft's surface must be smooth enough (surface roughness: $Ra \leq 0.4$ μm) to protect the variseal. The robot has already passed repeated sealing tests in a standard testing instrument.

Regarding electronic components, except for devices for driving, the gliding robotic dolphin is equipped with a group of low-power controllers, a variety of onboard sensors, and a wireless communication module. The main sensors for capturing motion states include an AHRS (Attitude and Heading Reference System) that offers attitude data, a depth sensor that measures diving depth, a GPS (Global Position System) module that locates the robot after surfacing, and a sonar for detecting obstacles ahead.

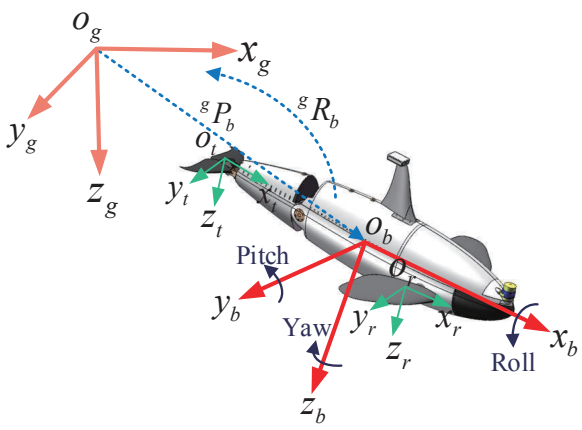

Fig. 3. Definition of coordinate frames.

3. 3D GLIDING MOTION MODELING

We derive the full-state dynamic model for 3D gliding motion in this section.

3.1 Coordinate Frames and Notations

The involved coordinate frames are defined as in Fig. 3. Let $C_g = o_g x_g y_g z_g$ denote the inertia frame with its axis z_g pointing to the gravity. Thereafter, a body-fixed frame $C_b = o_b x_b y_b z_b$ is assigned by placing its origin o_b at the robot's center of buoyancy (CB) and aligning plane $o_b x_b z_b$ with the robot's lateral symmetry plane. Considering the movable fin surfaces, we attach $C_t = o_t x_t y_t z_t$, $C_l = o_l x_l y_t z_l$, and $C_r = o_r x_r y_r z_r$ to the fluke, the left and right flippers, respectively.

In addition, we declare some notation convention for the following derivation. Regarding a physical tensor, the left superscript indicates the projection frame. For instance, ${}^gR_b$ and ${}^gP_b$ indicate the rotation matrix and position vector of C_b with respect to (w.r.t.) C_g. If a tensor is expressed in the frame where it is defined, its left superscript is sometimes omitted for convenience. For the cross product of two (3×1) vectors $\boldsymbol{a}$ and $\boldsymbol{b}$, a corresponding (3×3) skew-symmetric matrix $\hat{\boldsymbol{a}}$ is introduced: $\boldsymbol{a} \times \boldsymbol{b} = \hat{\boldsymbol{a}} \cdot \boldsymbol{b}$.

3.2 Kinematic Modeling

Let $V_b = (V_{bx},\ V_{by},\ V_{bz})^T$ and $\Omega_b = (\Omega_{bx},\ \Omega_{by},\ \Omega_{bz})^T$ denote the robot's linear and angular velocity w.r.t. frame C_b. The kinematic equations of the robot are as follows:

$$ {}^g\dot{P}_b = {}^gV_b = {}^gR_b V_b, \tag{1} $$

$$ {}^g\dot{R}_b = {}^gR_b \hat{\Omega}_b, \tag{2} $$

where the rotation matrix ${}^gR_b$ is parameterized by Euler angles (roll ϕ, pitch θ, yaw ψ) as

$$ {}^gR_b = \begin{pmatrix} \mathrm{c}\psi\mathrm{c}\theta & -\mathrm{s}\psi\mathrm{c}\phi+\mathrm{c}\psi\mathrm{s}\theta\mathrm{s}\phi & \mathrm{s}\psi\mathrm{s}\phi+\mathrm{c}\psi\mathrm{c}\phi\mathrm{s}\theta \\ \mathrm{s}\psi\mathrm{c}\theta & \mathrm{c}\psi\mathrm{c}\phi+\mathrm{s}\psi\mathrm{s}\theta\mathrm{s}\phi & -\mathrm{c}\psi\mathrm{s}\phi+\mathrm{s}\theta\mathrm{s}\psi\mathrm{c}\phi \\ -\mathrm{s}\theta & \mathrm{c}\theta\mathrm{s}\phi & \mathrm{c}\theta\mathrm{c}\phi \end{pmatrix}, $$

with c and s being short for cos and sin, respectively. The relation of linear accelerations w.r.t. frame C_g and frame C_b can be derived by derivative operation on (1):

$$ {}^g\dot{V}_b = ({}^gR_b\hat{\Omega}_b)V_b + {}^gR_b\dot{V}_b. \tag{3} $$

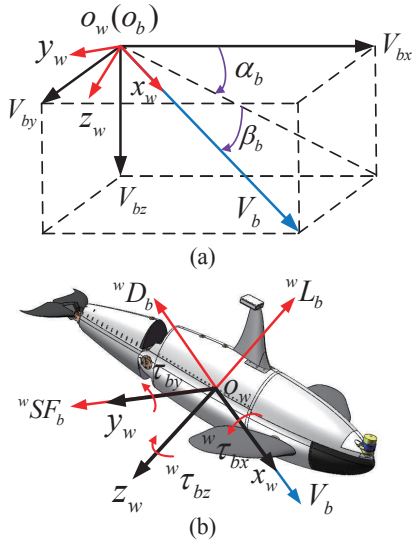

Fig. 4. Schematic illustration of the hydrodynamic forces and moments exerted on the body. (a) Wind axes; (b) Hydrodynamic forces and moments.

With regard to the flippers and the fluke, deflection angles should be considered. The fins' linear velocities w.r.t. the frames attached on them are formalized by:

$$ V_i = {}^iR_b(V_b + \Omega_b \times {}^bP_i) \quad (i = l,\ r,\ t), \tag{4} $$

where the indexes l, r, t indicate the left flipper, the right flipper, and the fluke, respectively; ${}^bP_i$ denotes a corresponding position vector; ${}^iR_b$ is a rotation matrix parameterized by a corresponding deflection angles δ_i:

$$ {}^iR_b = \begin{pmatrix} \cos\delta_i & 0 & \sin\delta_i \\ 0 & 1 & 0 \\ -\sin\delta_i & 0 & \cos\delta_i \end{pmatrix}. \tag{5} $$

3.3 Hydrodynamic Modeling

Hydrodynamic forces and moments are primary external forces exerted on the robot. They are generated by the interaction between the robot and the surrounding fluid. The quasi–steady model is adopted for analysis.

The hydrodynamic forces are related to the velocity and orientation of the robot relative to the current. For convenience, a new type of frame named wind axes is introduced to indicate the relative orientation. The wind axes assigned to the gliding robotic dolphin's body, as shown in Fig. 4, is denoted by $C_w = o_w x_w y_w z_w$ with the origin o_w overlapped with o_b and the axis x_w aligned with V_b. Thereafter, the relative orientation is essentially the rotation relation between frame C_w and frame C_b which can be parameterized by the attack angle α_b and the sideslip angle β_b:

$$ \alpha_b = \arctan(\frac{V_{bz}}{V_{bx}}),\ \beta_b = \arcsin(\frac{V_{by}}{\|V_b\|}). \tag{6} $$

As shown in Fig. 4(b), the hydrodynamic forces (moments) on the body include the lift force ${}^wL_b$, the drag force ${}^wD_b$, the sideslip force ${}^wSF_b$, and the moments about each axis of frame C_w, denoted by ${}^w\tau_{bx}$, ${}^w\tau_{by}$, and ${}^w\tau_{bz}$. The hydrodynamic force and moment vectors w.r.t. frame C_w are formalized below:

$$
\begin{aligned}
{}^{w}F_b &= \begin{pmatrix} -{}^{w}D_b \\ {}^{w}SF_b \\ -{}^{w}L_b \end{pmatrix} = \frac{1}{2}\rho S_b {V_b}^2 \begin{pmatrix} -C_{b,d}(\alpha_b) \\ C_{b,sf}(\beta_b) \\ -C_{b,l}(\alpha_b) \end{pmatrix} \\
{}^{w}\tau_b &= \begin{pmatrix} {}^{w}\tau_{bx} \\ {}^{w}\tau_{by} \\ {}^{w}\tau_{bz} \end{pmatrix} = \frac{1}{2}\rho S_b {V_b}^2 \begin{pmatrix} C_{b,\tau x}(\beta_b) \\ C_{b,\tau y}(\alpha_b) \\ C_{b,\tau z}(\beta_b) \end{pmatrix} + K_b\Omega_b
\end{aligned}, \quad (7)
$$

where ρ denotes the water density; S_b is the reference area of the body; $C_{b,d}$, $C_{b,sf}$, $C_{b,l}$, $C_{b,\tau x}$, $C_{b,\tau y}$, $C_{b,\tau z}$ indicate the corresponding hydrodynamic coefficients, which are related to α_b or β_b; K_b denotes the coefficient matrix of the rotational damping term. Further, the hydrodynamic forces and moments w.r.t. frame C_b are given by:

$$
F_b = {}^{b}R_w\, {}^{w}F_b,\ \tau_b = {}^{b}R_w\, {}^{w}\tau_b, \quad (8)
$$

where ${}^{w}R_b$ is a rotation matrix that depends on α_b and β_b:

$$
{}^{b}R_w = \begin{pmatrix} \cos\alpha_b\cos\beta_b & -\cos\alpha_b\sin\beta_b & -\sin\alpha_b \\ \sin\beta_b & \cos\beta_b & 0 \\ \sin\alpha_b\cos\beta_b & -\sin\alpha_b\sin\beta_b & \cos\alpha_b \end{pmatrix}. \quad (9)
$$

It should be noted that (6)–(9) only represent the hydrodynamic forces and moments on the body of the robot. The computational procedures for the flippers and the fluke are nearly the same, other than their deflection angles and action points should be considered. The velocity w.r.t. each fin's attached frame C_i (see (4)) is used when calculating the attack/slideslip angle:

$$
\alpha_i = \arctan(\frac{V_{iz}}{V_{ix}}),\ \beta_i = \arcsin(\frac{V_{iy}}{\|V_i\|}). \quad (10)
$$

The hydrodynamic forces w.r.t. frame C_i are calculated as in (7)–(8) first, and thereafter the ones w.r.t. frame C_b are deduced:

$$
\begin{pmatrix} {}^{b}F_i \\ {}^{b}\tau_i \end{pmatrix} = \begin{pmatrix} {}^{i}R_b & -{}^{i}R_b\, {}^{b}\hat{P}_i \\ \mathbf{0}_{3\times3} & {}^{i}R_b \end{pmatrix}^T \begin{pmatrix} F_i \\ \tau_i \end{pmatrix}. \quad (11)
$$

3.4 Dynamic Modeling

Another primary type of external forces are gravity and buoyancy. The buoyancy can be regulated by the buoyancy adjusting system as described in Section 2. Ideally, the buoyancy equals to the gravity when the oil volumes of the external and inner bladders are equivalent. The net buoyancy w.r.t. frame C_b can be obtained by:

$$
G_n = \frac{\rho}{\rho_o}(\frac{1}{2}m_o - m_{ex})g({}^{g}R_b{}^{T}\boldsymbol{k}), \quad (12)
$$

where m_o denotes the total oil mass; m_{ex} is the oil mass in the external bladder; ρ_o is the oil density; g is the gravitational acceleration; $\boldsymbol{k}$ indicates the unit vector along the z axis of frame C_g. The resultant moment by the gravity and buoyancy is formalized by:

$$
\tau_n = (m_b\hat{P}_b + m_o\hat{P}_o + m_m\hat{P}_m - \frac{\rho}{\rho_o}m_{ex}\hat{P}_{ex})g(R_b{}^{T}\boldsymbol{k}), \quad (13)
$$

where m_m is the movable mass; m_b is the robot's total mass excluding the movable mass and the oil mass; $\hat{P}_b$, $\hat{P}_o$, and $\hat{P}_m$ are corresponding centers of gravity (CGs) w.r.t. frame C_b.

Further, summing the external forces on the robot's each part yields the total external force:

$$
T_{ext} = \begin{pmatrix} F_b + {}^{b}F_l + {}^{b}F_r + {}^{b}F_t + G_n \\ \tau_b + {}^{b}\tau_l + {}^{b}\tau_r + {}^{b}\tau_t + \tau_n \end{pmatrix}. \quad (14)
$$

After deducing via Newton's law, we acquire the full-state dynamic model below for 3D gliding motion:

$$
\begin{aligned}
\begin{pmatrix} \dot{V}_b \\ \dot{\Omega}_b \end{pmatrix} &= \mathrm{M}^{-1}(\Pi + \Gamma_m + \Gamma_o + T_{ext}) \\
\Pi &= -\begin{pmatrix} \hat{\Omega}_b & \mathbf{0}_{3\times3} \\ \hat{V}_b & \hat{\Omega}_b \end{pmatrix} \mathrm{M} \begin{pmatrix} V_b \\ \Omega_b \end{pmatrix} \\
\Gamma_m &= m_m \begin{pmatrix} 2\dot{\hat{P}}_m\Omega_b - \ddot{P}_m \\ \hat{P}_m(2\dot{\hat{P}}_m\Omega_b - \ddot{P}_m) \end{pmatrix} \\
\Gamma_o &= m_o \begin{pmatrix} 2\dot{\hat{P}}_o\Omega_b - \ddot{P}_o \\ \hat{P}_o(2\dot{\hat{P}}_o\Omega_b - \ddot{P}_o) \end{pmatrix}
\end{aligned}, \quad (15)
$$

where Π indicates the Coriolis-centrifugal force; Γ_m and Γ_o denote the forces caused by the CG shift of the movable mass and the oil bladders; M is the total inertia matrix, composed of the inertia matrix of the robot M_{dl} and the added inertia matrix M_{ad} from the surrounding water:

$$
\begin{aligned}
\mathrm{M} &= M_{dl} + M_{ad} \\
M_{ad} &= \begin{pmatrix} M_f & D_f{}^{T} \\ D_f & J_f \end{pmatrix} \\
M_{dl} &= \begin{pmatrix} (m_b + m_m + m_o)I_{3\times3} & D^T \\ D & J \end{pmatrix} \\
D &= m_b\hat{P}_b + m_o\hat{P}_o + m_m\hat{P}_m \\
J &= J_b - m_r\hat{P}_b\hat{P}_b - m_o\hat{P}_o\hat{P}_o - m_m\hat{P}_m\hat{P}_m
\end{aligned}, \quad (16)
$$

where J_b is the rotational inertial caused by the distribution of m_b relative to its CG.

Definitely, we formalize the CG shift process of the movable mass and the oil bladders in (15) as follows:

$$
\begin{aligned}
\dot{P}_o &= \sigma_o v_o(P_{in} - P_{ex})/m_o \\
\dot{P}_m &= V_m
\end{aligned}, \quad (17)
$$

where V_m is the velocity of the movable mass, P_{in} denotes the CG of the inner bladder, σ_o and v_o are the pump's displacement and rotation speed respectively. Actually, we have assumed that $\ddot{P}_m = 0$ and $\ddot{P}_o = 0$ for convenience, since the pump and the movable mass remain still at most time or occasionally move uniformly, and their start-stop processes are indeed rapid.

4. SIMULATIONS AND EXPERIMENTS

Simulations are carried out based on the built dynamic model to analyze the 3D gliding motion. We also conduct experiments to validate the gliding performance of the robot and the effectiveness of the model.

4.1 Simulation Results

The involved physical parameters are listed in Table 1. We measure the mass properties directly, whilst the position vectors and the angular inertia matrix are obtained from the mechanical model. Besides, computational fluid dynamics (CFD) simulations (Wu et al. (2015a)) are implemented to compute the hydrodynamic coefficients under different attack/sideslip angles. Considering the fins are movable, we treat with the robot's body, flippers, and fluke separately during the CFD simulations.

A 2D gliding case is simulated first, and the motion states are shown in Fig. 5. Initially, the robot stay static with zero

Table 1. Physical parameters of the gliding robotic dolphin

Symbol	Value	Symbol	Value
m_b	53.7 Kg	m_m	2.86 Kg
m_o	1.54 Kg	ρ	998.2 Kg/m^3
ρ_o	800 Kg/m^3	σ_o	2.5×10^{-7} m^3/r
P_b	$[0.0017,\ 0,\ 0.02]^T$	P_{in}	$[0.3696,\ 0,\ 0.0308]^T$
P_{ex}	$[0.5206,\ 0,\ 0.0308]^T$	P_{m0}	$[-0.0964,\ 0,\ -0.065]^T$
P_l	$[0.29,\ -0.176,\ 0.049]^T$	P_r	$[0.29,\ 0.176,\ 0.049]^T$
P_t	$[-0.755,\ 0,\ -0.012]^T$	P_d	$[0.548,\ 0,\ -0.067]^T$
M_f	diag$\{1.2,\ 10.8,\ 12.5\}$	D_f	$\mathbf{0}_{3\times3}$
J_f	diag$\{0.036,\ 1.66,\ 2.46\}$	g	9.8 m/s^2

Note: all the parameters are quantified with the international system of units. P_{m0} indicates the initial position of the movable mass.

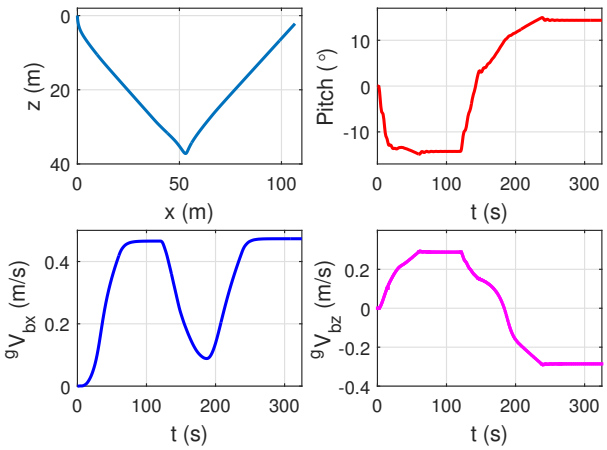

Fig. 5. Motion states when the robot glides in the vertical plane.

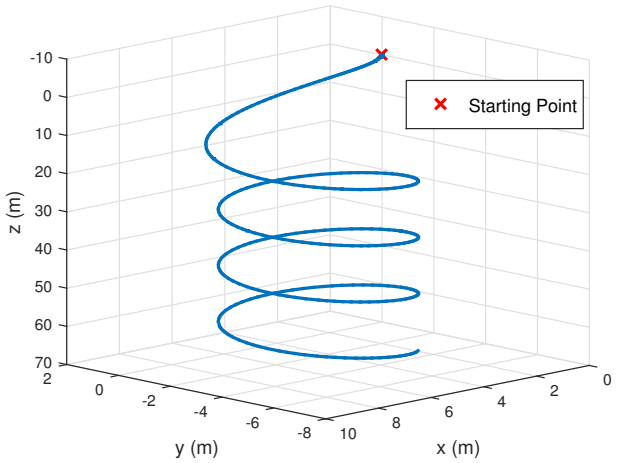

Fig. 6. 3D path of the spiraling motion.

net-buoyancy and attitude. At $t = 1$ s, the pump starts to suck in oil at a speed of $v_o = 50$ rps (rps for revolutions per second). At the same time, the movable mass pushes ahead for 4 cm at 3 mm/s to make the robot nose down. As a result, the robot begins to dive and glide forward. At $t = 120$ s, the robot is commanded to surface: the pump ejects oil in the inner bladder also at $v_o = 50$ rps, and the

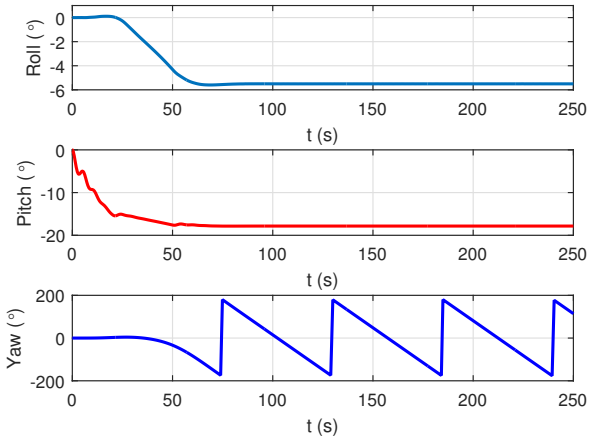

Fig. 7. Attitude during the spiraling motion.

movable mass shifts back for 8 cm at 3 mm/s. Owing to the pump's small displacement, the switching point actually occurs at $t = 183$ s. Consequently, the sawtooth-like path arises, as shown in Fig. 5. The equilibrium states can be observed from the simulation. In the steady gliding stage, the pitch angle, the attack angle, and the gliding angle stay around $\pm15°$, $\pm18°$, and $\pm33°$, respectively. It reveals that the mechanical design of the robot pursues a relatively high gliding speed and simultaneously considers gliding efficiency.

By virtue of the flippers, the robot can perform 3D spiraling motion. To yield a spiraling case, the left flipper maintains a deflection angle of 30°, while the other actuators execute the same actions with the 2D gliding case above for diving. The consequent 3D path and attitude are plotted in Figs. 6–7, respectively. The differential action of the flippers generates asymmetric hydrodynamics on the left and right sides, and thereby the turning motion appears. The concomitant roll movement shown in Fig. 7 rotates the lift and drag forces out of the the vertical plane, which provides the centripetal force for circular motion in the steady gliding stage. Hence, the projection of the 3D path in the steady gliding stage on the $x - y$ plane is essentially circular. During the circular motion, the yaw angle decreases from 180° to −180° uniformly and repeatedly.

4.2 Experimental Results

Experiments are implemented to validate the gliding motion of the robot in a diving training pool (length: 15 m, width: 6 m, depth: 7.5 m). A snapshot sequence captured from a diving-surfacing round is shown in Fig. 8. The observed gliding trajectory is consistent with the theoretical shape. The start-up process and the switching process between diving and surfacing cost a long time since the buoyancy adjusting system is slow. Owing to the limitation of the pool's size, it is impossible to reach the equilibrium states with all the oil being sucked or ejected in a diving-surfacing round. Thereby, we try to release the robot after all the oil is sucked, in order to seek the equilibrium states. It is observed that the horizontal speed during steady gliding stage reaches about 0.4 m/s, which is very close to the simulated one shown in Fig. 5.

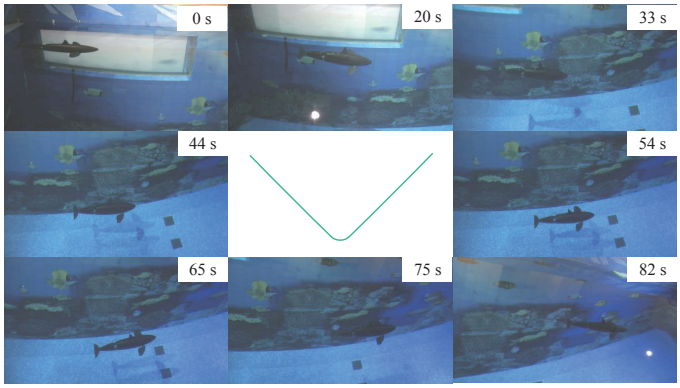

Fig. 8. Snapshots of a diving-surfacing round.

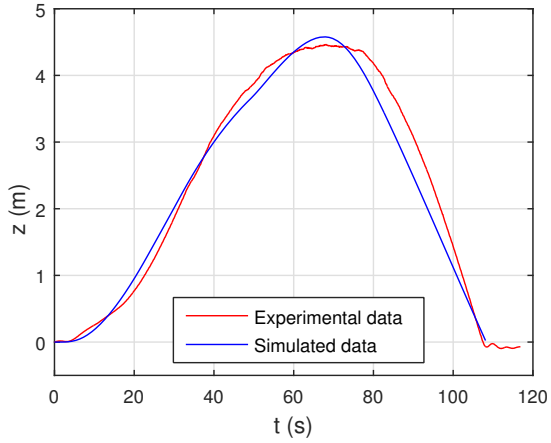

Fig. 9. The simulated and experimental depth.

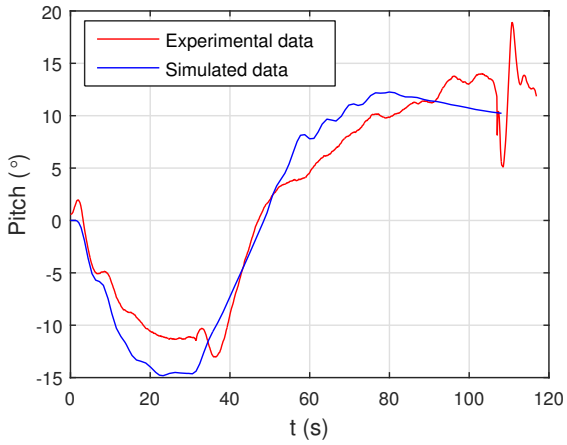

Fig. 10. The simulated and experimental pitch angle.

The onboard sensors collect realtime depth and attitude data during motion. We compare the simulated and experimental data of a diving-surfacing round, as shown in Figs. 9–10. The robot is commanded to surface when the diving depth exceeds 2 m, while the actual switching depth is 4.4 m. When the robot comes out of the water surface, it fluctuates up and down slightly owing to its inertia, leading to the undulation of the experimental depth and pitch angle observed from 105 s to the end. The comparison reveals the effectiveness of the built dynamic model for gliding motion to some extent, despite of the small deviations between the simulated and experimental data. The discrepancy of hydrodynamics, the slight yaw movement caused by CG misalignments or asymmetry of hydrodynamic structures, and some other unmodelled factors may contribute to the deviations.

5. CONCLUSIONS AND FUTURE WORK

This paper has presented the mechatronic design and 3D motion modeling of a gliding robotic dolphin with a nominal diving depth of 300 m. In order to endow the robot with both high maneuverability and long endurance simultaneously, we have integrated propulsion modes of bio-inspired robotic dolphin and traditional underwater gliders, via introducing a buoyancy adjusting mechanism on the basis of a robotic dolphin. To achieve a large diving depth, we have implemented particular design on mechanical seal and compressive strength. In addition, a full-state dynamic model for 3D gliding motion has been established for motion analysis. The robot's controllable flippers and fluke have been considered specially in the dynamic model. Simulations have been conducted to analyze the 3D gliding motion. Further, the completed experiments have validated the robot's gliding performance and the effectiveness of the dynamic model.

In the future, field tests will be carried out for further validation. Effort will also be put on investigating closed-loop attitude control via the robot's fins.

REFERENCES

Eriksen, C.C., Osse, T.J., and et al. (2001). Seaglider: A long-range autonomous underwater vehicle for oceanographic research. *IEEE Journal of Oceanic Engineering*, 26(4), 424–436.

Leonard, N.E., Paley, D.A., and et al. (2010). Coordinated control of an underwater glider fleet in an adaptive ocean sampling field experiment in monterey bay. *Journal of Field Robotics*, 27(6), 718–740.

Nakashima, M., Tsubaki, T., and Ono, K. (2006). Three-dimensional movement in water of the dolphin robot. *Journal of Robotics and Mechatronics*, 18(3), 347–355.

Schofield, O., Kohut, J., and et al. (2007). Slocum gliders: Robust and ready. *Journal of Field Robotics*, 24(6), 473–486.

Weihs, D. (2002). Dynamics of dolphin porpoising revisited. *Integrative and Comparative Biology*, 42(5), 1071–1078.

Wu, Z., Yu, J., and et al. (2015a). Mechatronic design and implementation of a novel gliding robotic dolphin. In *IEEE International Conference on Robotics and Biomimetics*, 267–272.

Wu, Z., Yu, J., and et al. (2015b). Towards an esox lucius inspired multimodal robotic fish. *Science China Information Sciences*, 58(5), 1–13.

Yu, J., Su, Z., and et al. (2012). Control of yaw and pitch maneuvers of a multilink dolphin robot. *IEEE Transactions on Robotics*, 28(2), 318–329.

Yu, J., Su, Z., and et al. (2016). An integrative control method for bio-inspired dolphin leaping: Design and experiments. *IEEE Transactions on Industrial Electronics*, 63(5), 3108–3116.